

# Studies of granularity of a hadronic calorimeter for tens-of-TeV jets at a 100 TeV $pp$ collider

C.-H. Yeh<sup>a</sup>, S.V. Chekanov<sup>b</sup>, A.V. Kotwal<sup>c</sup>, J. Proudfoot<sup>b</sup>, S. Sen<sup>c</sup>, N.V. Tran<sup>d</sup>,  
S.-S. Yu<sup>a</sup>

<sup>a</sup> *Department of Physics, National Central University, Chung-Li, Taoyuan City 32001, Taiwan*

<sup>b</sup> *HEP Division, Argonne National Laboratory, 9700 S. Cass Avenue, Argonne, IL 60439, USA.*

<sup>c</sup> *Department of Physics, Duke University, USA*

<sup>d</sup> *Fermi National Accelerator Laboratory*

<sup>e</sup> *Department of Physics, Michigan State University, 220 Trowbridge Road, East Lansing, MI 48824*

---

## Abstract

Jet substructure variables for hadronic jets with transverse momenta in the range from 2.5 TeV to 20 TeV were studied using several designs for the spatial size of calorimeter cells. The studies used the full Geant4 simulation of calorimeter response combined with realistic reconstruction of calorimeter clusters. In most cases, the results indicate that the performance of jet-substructure reconstruction improves with reducing cell size of a hadronic calorimeter from  $\Delta\eta \times \Delta\phi = 0.087 \times 0.087$  to  $0.022 \times 0.022$ .

*Keywords:* multi-TeV physics,  $pp$  collider, future hadron colliders, FCC, SppC

---

## 1. Introduction

Particle collisions at energies beyond those attained at the LHC will lead to many challenges for detector technologies. Future circular  $pp$  colliders such as the European initiatives, high-energy LHC (HE-LHC) and FCC-hh [1] and the Chinese initiative, SppC [2] will measure high-momentum bosons ( $W$ ,  $Z$ ,  $H$ ) and top quarks with highly-collimated decay products that form jets. Jet substructure techniques are used to identify such boosted particles, and thus can maximize the physics potential of the future colliders.

The reconstruction of jet substructure variables for collimated jets with transverse momenta above 10 TeV requires an appropriate detector design. The most important detector systems for reconstruction of such jets are tracking and calorimetry. Recently, a number of studies [3, 4, 5] have been discussed using various fast simulation tools, such as Delphes [6], in which momenta of particles are smeared to mimic detector response.

A major step towards the usage of full Geant4 simulation to verify the granularity requirements for calorimeters was made in [7]. These studies have illustrated a significant impact of granularity of electromagnetic (ECAL) and hadronic (HCAL) calorimeters

---

*Email addresses:* jwzuzelski18@gmail.com (C.-H. Yeh), chekanov@anl.gov (S.V. Chekanov), ashutosh.kotwal@duke.edu (A.V. Kotwal), proudfoot@anl.gov (J. Proudfoot), sourav.sen@duke.edu (S. Sen), ntran@fnal.gov (N.V. Tran), syu@cern.ch (S.-S. Yu)

on the cluster separation between two particles. It was concluded that high granularity is essential in resolving two close-by particles for energies above 100 GeV.

This paper takes the next step in understanding this problem in terms of high-level quantities typically used in physics analyses. Similar to the studies presented in [7], this paper is based on a full Geant4 simulation with realistic jet reconstruction.

## 2. Simulation of detector response

The description of the detector and software used for this study is discussed in [7]. We use the SiFCC detector geometry with a software package that provides a versatile environment for simulations of detector performance, testing new technology options, and event reconstruction techniques for future 100 TeV colliders.

The baseline detector discussed in [7] uses a steel-scintillator hadronic calorimeter with a transverse cell size of  $5 \times 5 \text{ cm}^2$ , which corresponds to  $\Delta\eta \times \Delta\phi = 0.022 \times 0.022$ , where  $\eta$  is the pseudorapidity,  $\eta \equiv -\ln \tan(\theta/2)$ , and  $\phi$  is the azimuthal angle. The depth of the HCAL in the barrel region is 11.25 interaction lengths ( $\lambda_I$ ). The HCAL has 64 longitudinal layers in the barrel and the endcap regions.

In addition to the baseline HCAL geometry, several geometry variations were considered. We used the HCAL with transverse cell size of  $20 \times 20 \text{ cm}^2$ ,  $2 \times 2 \text{ cm}^2$  and  $1 \times 1 \text{ cm}^2$ . In the terms of  $\Delta\eta \times \Delta\phi$ , such cell sizes correspond to  $0.087 \times 0.087$ ,  $0.0087 \times 0.0087$  and  $0.0043 \times 0.0043$ , respectively.

The GEANT4 (version 10.3) [8] simulation of calorimeter response was followed by the full reconstruction of calorimeter clusters formed by the Pandora algorithm [9, 10]. Calorimeter clusters were built from calorimeter hits in the ECAL and HCAL after applying the corresponding sampling fractions. No other corrections are applied. Hadronic jets were reconstructed with the FASTJET package [11] using the anti- $k_T$  algorithm [12] with a distance parameter of 0.5.

In the following discussion, we use the simulations of a heavy  $Z'$  boson, a hypothetical gauge boson that arises from extensions of the electroweak symmetry of the Standard Model. The  $Z'$  bosons were simulated with the masses  $M = 5, 10, 20$  and  $40 \text{ TeV}$ . The lowest value represents a typical mass that is within the reach of the LHC experiments. The resonance mass of  $40 \text{ TeV}$  represents the physics reach for a 100 TeV collider. The  $Z'$  bosons are forced to decay to two light-flavor quark ( $q\bar{q}$ ),  $W^+W^-$  or  $t\bar{t}$  final states, where the  $W$  bosons and  $t$  quarks decay hadronically. In these scenarios, two highly-boosted jets are produced, which are typically back-to-back in the laboratory frame. The typical transverse momenta of the jets are  $\simeq M/2$ . The main difference between the considered decay modes lies in the different jet substructures. In the case of the  $q\bar{q}$  decays, jets do not have any internal structure. In the case of the  $W^+W^-$  final state, each jet has two subjets because of the decay  $W \rightarrow q\bar{q}$ . In the case of hadronic top decays, jets have three subjets due to the decay  $t \rightarrow W^+ b \rightarrow q\bar{q}b$ . The signal events were generated using the PYTHIA8 generator with the default settings, ignoring interference with SM processes. The event samples used in this paper are available from the HepSim database [13].

### 58 3. Studies of jet properties

59 We consider several variables that characterize jet substructure using different  
60 calorimeter granularities. The question we want to answer is, how closely the re-  
61 constructed jet substructure variables reflect the input “truth” values that are recon-  
62 structed using particles directly from the PYTHIA8 generator.

63 In this study we use the jet effective radius and jet splitting scales as benchmark  
64 variables to study jet substructure properties. The effective radius is the average of the  
65 energy-weighted radial distance  $\delta R_i$  in  $\eta - \phi$  space of jet constituents. It is defined as  
66  $(1/E) \sum_i e_i \delta R_i$ , where  $E$  is the energy of the jet and  $e_i$  is the energy of a calorimeter  
67 constituent cluster  $i$  at the distance  $\delta R_i$  from the jet center. The sum runs over all  
68 constituents of the jet. This variable has been studied for multi-TeV jets in Ref. [14].  
69 A jet  $k_T$  splitting scale [15] is defined as a distance measure used to form jets by the  
70  $k_T$  recombination algorithm [16, 17]. This variable has been studied by ATLAS [18],  
71 and more recently in the context of 100 TeV physics [14]. The splitting scale is defined  
72 as  $\sqrt{d_{12}} = \min(p_T^1, p_T^2) \times \delta R_{12}$  [18] at the final stage of the  $k_T$  clustering, where two  
73 subjects are merged into the final jet.

74 Figures 1 and 2 show the distributions of the jet effective radius and jet splitting  
75 scale for different jet transverse momenta and HCAL granularities. The reconstructed-  
76 level distributions disagree significantly with the distributions reconstructed using truth-  
77 level particles. The distributions reconstructed with cell size  $1 \times 1 \text{ cm}^2$  are closest to the  
78 truth-level variables. The distributions reconstructed using the cell size of  $20 \times 20 \text{ cm}^2$ ,  
79 show the largest discrepancy with the truth-level variables. Note that, in terms of  
80 similarity of reconstructed distributions to the truth-level distributions, there is no  
81 significant difference between  $5 \times 5 \text{ cm}^2$ ,  $2 \times 2 \text{ cm}^2$  and  $1 \times 1 \text{ cm}^2$  cell sizes.

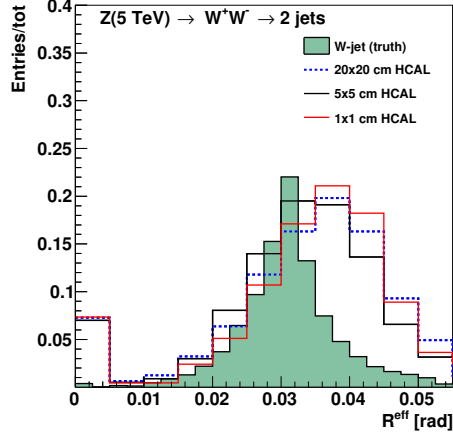
82 This study confirms the baseline SiFCC detector geometry [7] that uses  $5 \times 5 \text{ cm}^2$   
83 HCAL cells, corresponding to  $\Delta\eta \times \Delta\phi = 0.022 \times 0.022$ . Similar HCAL cell sizes,  
84  $0.025 \times 0.025$ , were recently adopted for the baseline FCC-hh detector [19, 20] planned  
85 at CERN. Before the publication [7], such a choice for the HCAL cells was motivated  
86 by the studies of jet substructure using a fast detector simulation of boosted jets. In  
87 addition to the improvements in physics performance, the smaller HCAL cells reduce  
88 the required dynamic range for signal reconstruction [4], and thus can simplify the  
89 calorimeter readout.

90 It should be noted that the ATLAS and CMS detectors use the HCAL cell sizes in  
91 the barrel region which are close to  $\Delta\eta \times \Delta\phi = 0.087 \times 0.087$ . According to this study,  
92 such HCAL cell sizes are not optimal in terms of performance for tens-of-TeV jets.

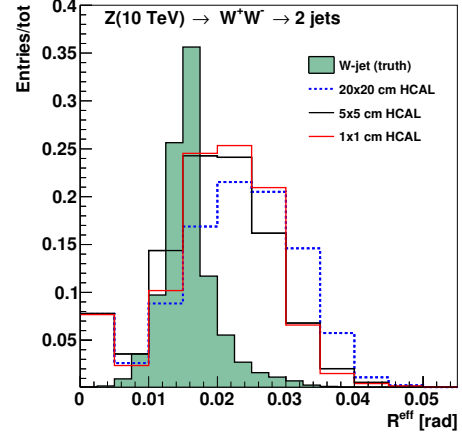
93 In the following sections we consider several other physics-motivated variables that  
94 can shed light on the performance of the HCAL for tens-of-TeV jets.

### 95 4. Detector performance with soft drop mass

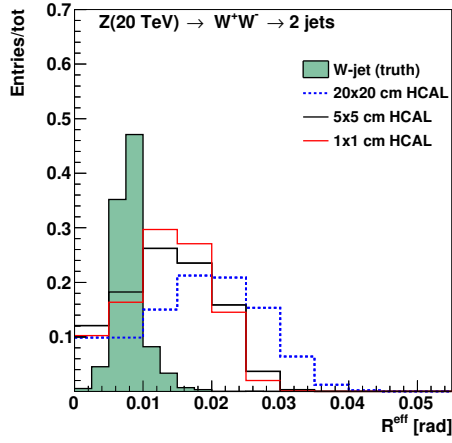
96 In this section, we use the jet mass computed with a specific algorithm, soft drop  
97 declustering, to study the performance with various detector cell sizes and resonance  
98 masses.



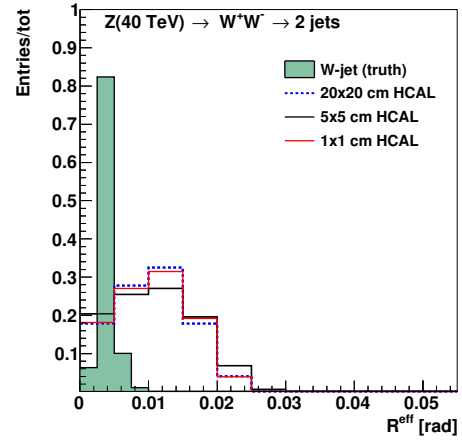
(a) 5 TeV



(b) 10 TeV

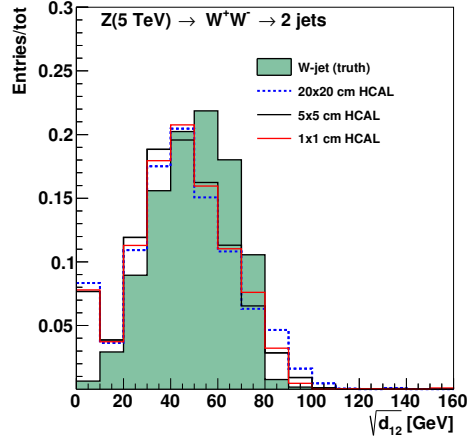


(c) 20 TeV

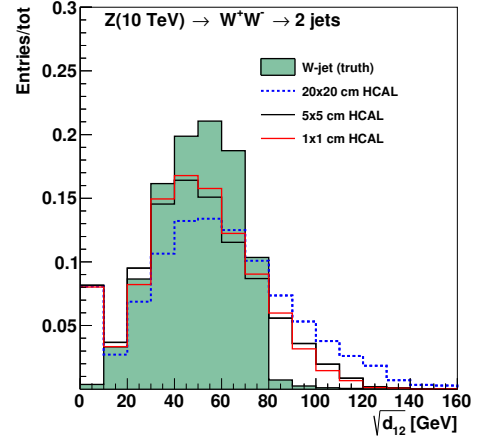


(d) 40 TeV

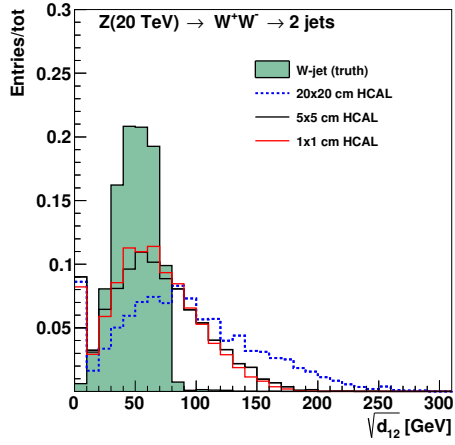
Figure 1: Jet effective radius for different jet transverse momenta and HCAL granularities.



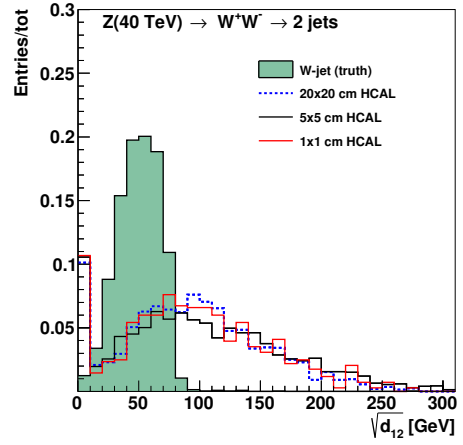
(a) 5 TeV



(b) 10 TeV



(c) 20 TeV



(d) 40 TeV

Figure 2: Jet splitting scale for different jet transverse momenta and HCAL granularity.

#### 99 4.1. The technique of soft drop declustering

100 The soft drop declustering [21] is a grooming method that removes soft wide-  
 101 angle radiation from a jet. The constituents of a jet  $j_0$  are first reclustered using  
 102 the Cambridge-Aachen (C/A) algorithm [22, 23]. Then, the jet  $j_0$  is broken into two  
 103 subjets  $j_1$  and  $j_2$  by undoing the last stage of C/A clustering. If the subjets pass  
 104 the following soft drop condition, jet  $j_0$  is the final soft-drop jet. Otherwise, the algo-  
 105 rithm redefines  $j_0$  to be the subjet with larger  $p_T$  (among  $j_1$  and  $j_2$ ) and iterates the  
 106 procedure. The condition is,

$$\frac{\min(p_{T1}, p_{T2})}{p_{T1} + p_{T2}} > z_{\text{cut}} \left( \frac{\Delta R_{12}}{R_0} \right)^\beta, \quad (1)$$

107 where  $p_{T1}$  and  $p_{T2}$  are the transverse momenta of the two subjets,  $z_{\text{cut}}$  is soft drop  
 108 threshold,  $\Delta R_{12}$  is the distance between the two subjets in the rapidity-azimuthal  
 109 plane ( $y$ - $\phi$ ),  $R_0$  is the characteristic radius of the original jet, and  $\beta$  is the angular  
 110 exponent.

111 In our study, we compare the HCAL performance for the soft drop mass with  $\beta = 0$   
 112 and  $\beta = 2$ . For  $\beta = 0$ , the soft drop condition depends only on the  $z_{\text{cut}}$ . For  $\beta = 2$ , the  
 113 condition depends on the angular distance between the two subjets and  $z_{\text{cut}}$  and the  
 114 algorithm becomes infrared and collinear safe.

#### 115 4.2. Analysis method

116 We employ the following method to quantify the detector performance and deter-  
 117 mine the cell size that gives the best separation between signal and background. For  
 118 each configuration of detector and resonance mass, we draw the receiver operating char-  
 119 acteristic (ROC) curves in which the  $x$ -axis is the signal efficiency ( $\epsilon_{\text{sig}}$ ) and  $y$ -axis is  
 120 the inverse of the background efficiency ( $1/\epsilon_{\text{bkg}}$ ). In order to scan the efficiencies of  
 121 soft drop mass cuts, we vary the mass window as follows. We center the initial window  
 122 on the median of the signal histogram, and increase its width symmetrically left and  
 123 right in bins of 5 GeV. If one side of the mass window reaches the boundary of the  
 124 mass histogram, we increase the width on the other side. For each mass window, the  
 125 corresponding efficiencies  $\epsilon_{\text{sig}}$  and  $\epsilon_{\text{bkg}}$  give a point on the ROC curve.

#### 126 4.3. Results and conclusion

127 Figures 3, 5, 7 and 9 show the distributions for the soft drop mass for  $\beta = 0$  and  
 128  $\beta = 2$  with different resonance masses and detector cell sizes; the signals considered are  
 129 the  $Z' \rightarrow WW$  and  $Z' \rightarrow t\bar{t}$  processes. Figures 4, 6, 8 and 10 show the corresponding  
 130 ROC curves for different detector cell sizes and resonance masses.

131 These studies show that the reconstruction of soft drop mass improves with de-  
 132 creasing HCAL cell sizes. Figures 4 and 6 show that for  $\beta = 0$  the smallest detector  
 133 cell size,  $1 \times 1 \text{ cm}^2$ , has the best separation power at resonance masses of 5, 10, and  
 134 20 TeV when the signal is the  $Z' \rightarrow WW$  process, and at resonance masses of 10 and 20  
 135 TeV when the signal is the  $Z' \rightarrow t\bar{t}$  process. On the contrary, Figs. 8 and 10 show that  
 136 for  $\beta = 2$  the smallest detector cell size does not have improvements in the separation  
 137 power when compared with larger cell sizes. In fact, the performance for the three cell  
 138 sizes is similar. In addition, sometimes bigger cell sizes,  $5 \times 5 \text{ cm}^2$  or even  $20 \times 20 \text{ cm}^2$   
 139 have the best separation power.

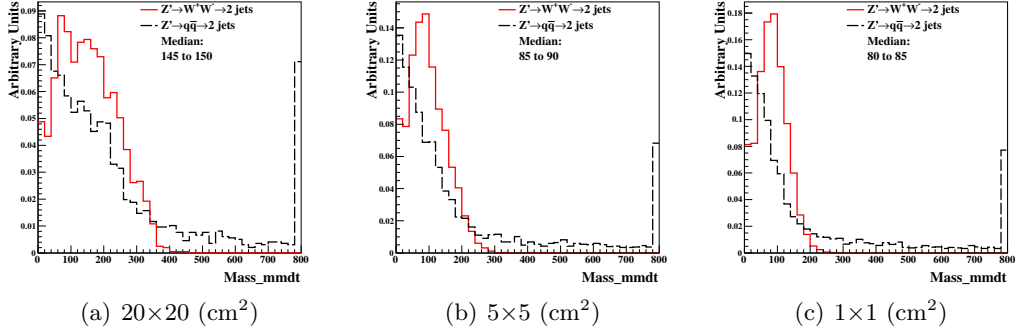


Figure 3: Distributions of soft drop mass for  $\beta=0$ , with  $M(Z') = 20$  TeV and three different detector cell sizes:  $20 \times 20$ ,  $5 \times 5$  and  $1 \times 1$   $\text{cm}^2$ . The signal (background) process is  $Z' \rightarrow WW$  ( $Z' \rightarrow q\bar{q}$ ).

Note that the separation between ROC curves depends on the physics variable and on the boost of the top quarks or the  $W$  bosons. For example, the similarity between the ROC curves shown in Fig. 6(a) is due to the insufficient boost of the top quarks. On the other hand, Fig. 6(d) does not show a difference between the ROC curves because the boost is too high.

We also find that the soft drop mass with  $\beta = 0$  has better performance for distinguishing signal from background than with  $\beta = 2$ . Therefore, we will apply requirements on the soft drop mass with  $\beta = 0$  when studying the other jet substructure variables.

## 5. Detector performance with jet substructure variables

In this section, we use several jet substructure variables to study the performance with various detector cell sizes and resonance masses.

### 5.1. $N$ -subjettiness

The variable  $N$ -subjettiness [24], denoted by  $\tau_N$ , is designed to “count” the number of subjet(s) in a large radius jet in order to separate signal jets from decays of heavy bosons and background jets from QCD processes.  $\tau_N$  is the  $p_T$ -weighted angular distance between each jet constituent and the closest subjet axis:

$$\tau_N = \frac{1}{d_0} \sum_k p_{T,k} \min\{\Delta R_{1,k}, \Delta R_{2,k}, \dots, \Delta R_{N,k}\}, \quad (2)$$

with a normalization factor  $d_0$ :

$$d_0 = \sum_k p_{T,k} R_0.$$

The  $k$  index runs over all constituent particles in a given large radius jet,  $p_{T,k}$  is the transverse momentum of each individual constituent,  $\Delta R_{j,k} = \sqrt{(\Delta y)^2 + (\Delta \phi)^2}$  is the

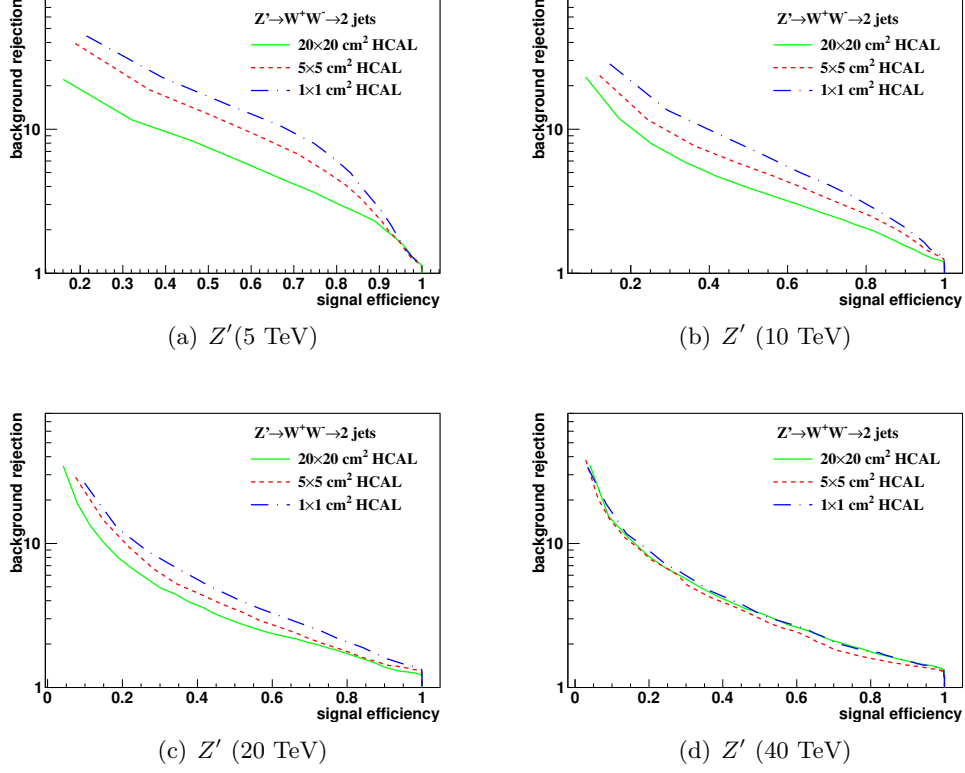


Figure 4: The ROC curves of soft drop mass selection for  $\beta=0$  with resonance masses of 5, 10, 20 and 40 TeV. Three different detector cell sizes are compared:  $20 \times 20$ ,  $5 \times 5$ , and  $1 \times 1$   $\text{cm}^2$ . The signal (background) process is  $Z' \rightarrow WW$  ( $Z' \rightarrow q\bar{q}$ ).

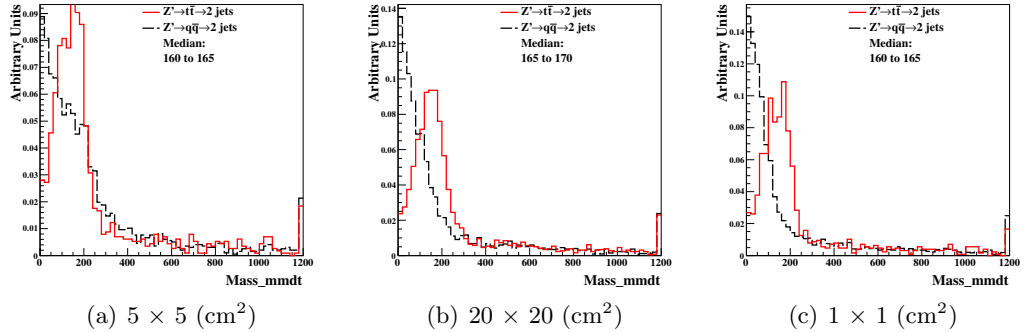


Figure 5: Distributions of soft drop mass for  $\beta=0$ , with  $M(Z') = 20$  TeV and three different detector cell sizes:  $20 \times 20$ ,  $5 \times 5$ , and  $1 \times 1$   $\text{cm}^2$ . The signal (background) process is  $Z' \rightarrow t\bar{t}$  ( $Z' \rightarrow q\bar{q}$ ).



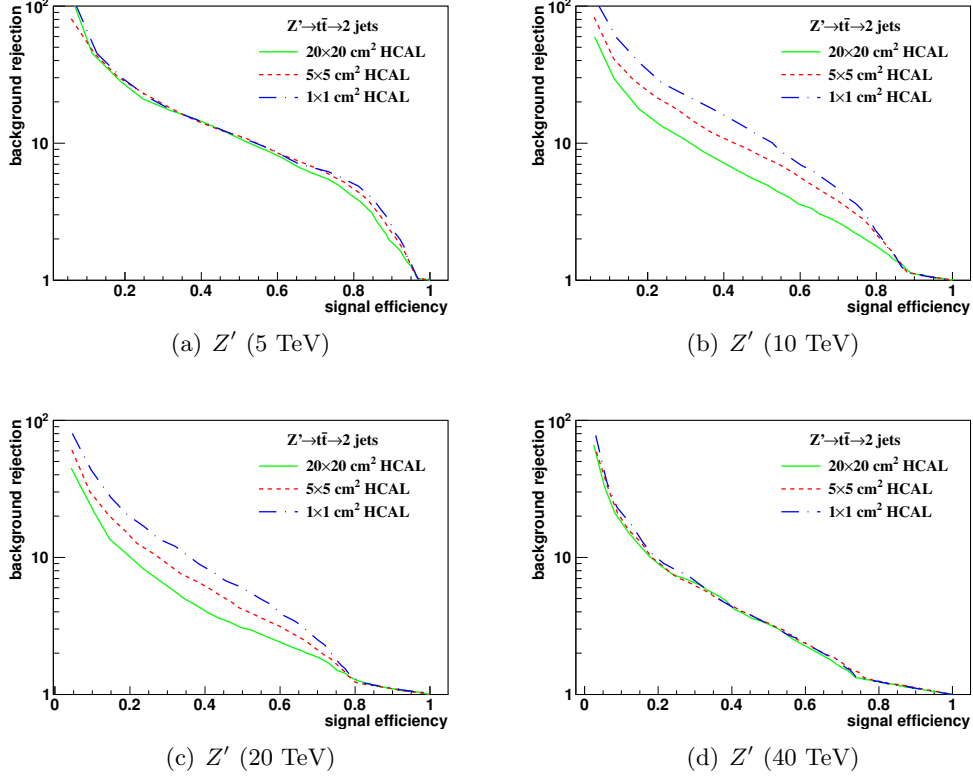


Figure 6: The ROC curves of soft drop mass selection for  $\beta=0$  with resonance masses of 5, 10, 20 and 40 TeV. Three different detector cell sizes are compared:  $20 \times 20$ ,  $5 \times 5$ , and  $1 \times 1$   $\text{cm}^2$ . The signal (background) process is  $Z' \rightarrow t\bar{t}$  ( $Z' \rightarrow q\bar{q}$ ).

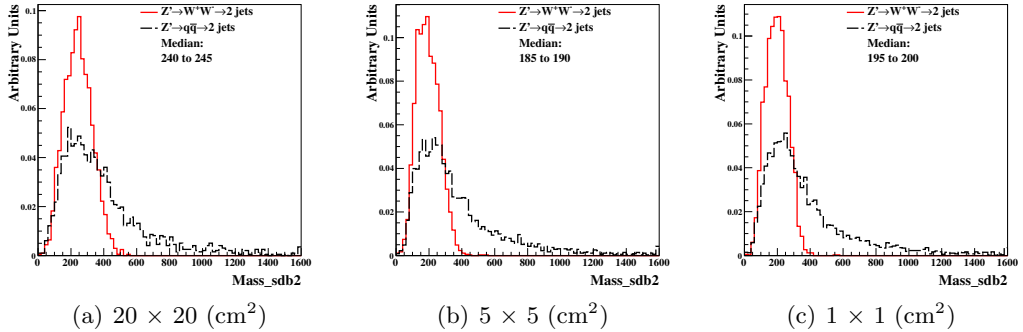


Figure 7: Distributions of soft drop mass for  $\beta = 2$ , with  $M(Z') = 20$  TeV and three different detector cell sizes:  $20 \times 20$ ,  $5 \times 5$  and  $1 \times 1$   $\text{cm}^2$ . The signal (background) process is  $Z' \rightarrow WW$  ( $Z' \rightarrow q\bar{q}$ ).

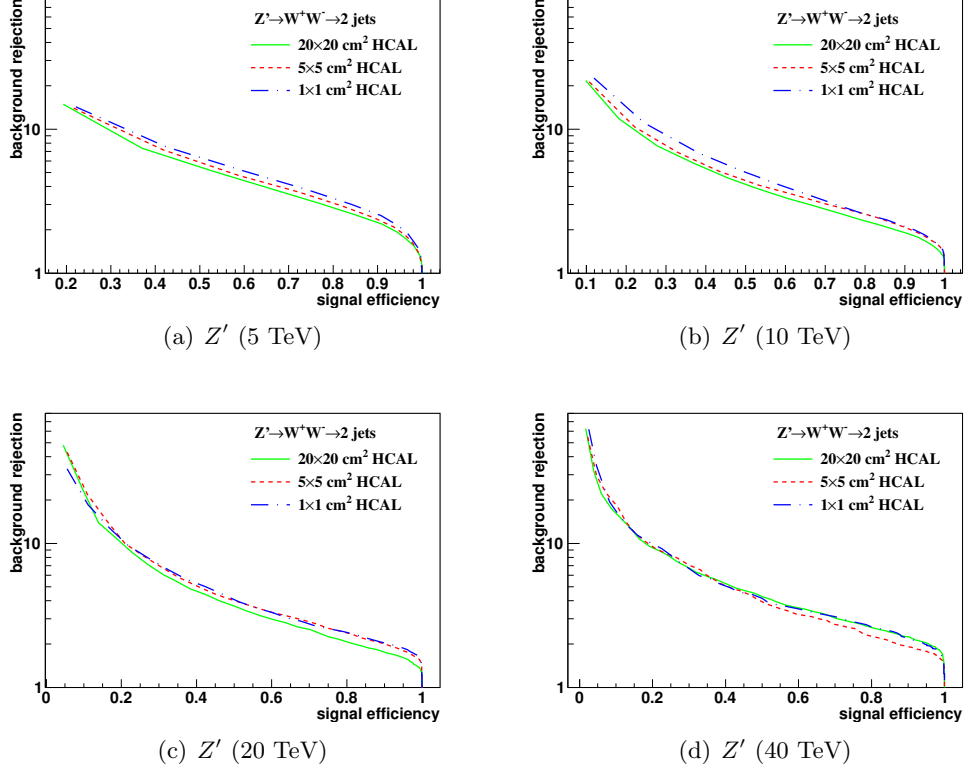


Figure 8: The ROC curves of soft drop mass selection for  $\beta = 2$  with resonance masses of 5, 10, 20 and 40 TeV. Three different detector cell sizes are compared:  $20 \times 20$ ,  $5 \times 5$ , and  $1 \times 1$   $\text{cm}^2$ . The signal (background) process is  $Z' \rightarrow WW$  ( $Z' \rightarrow q\bar{q}$ ).

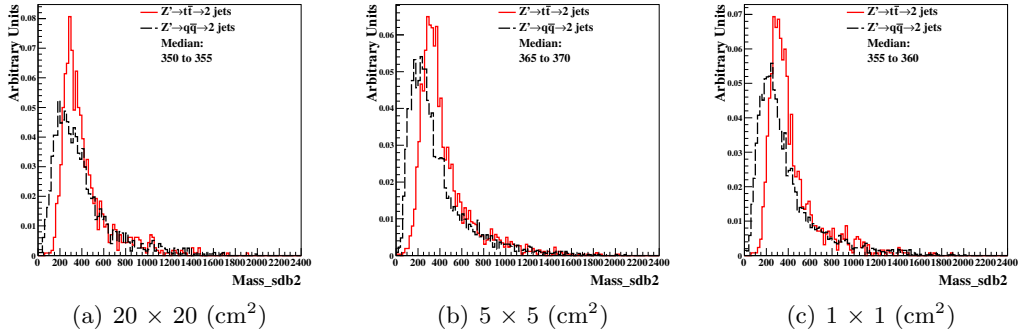


Figure 9: Distributions of soft drop mass for  $\beta = 2$ , with  $M(Z') = 20$  TeV and three different detector cell sizes:  $20 \times 20$ ,  $5 \times 5$ , and  $1 \times 1$   $\text{cm}^2$ . The signal (background) process is  $Z' \rightarrow t\bar{t}$  ( $Z' \rightarrow q\bar{q}$ ).

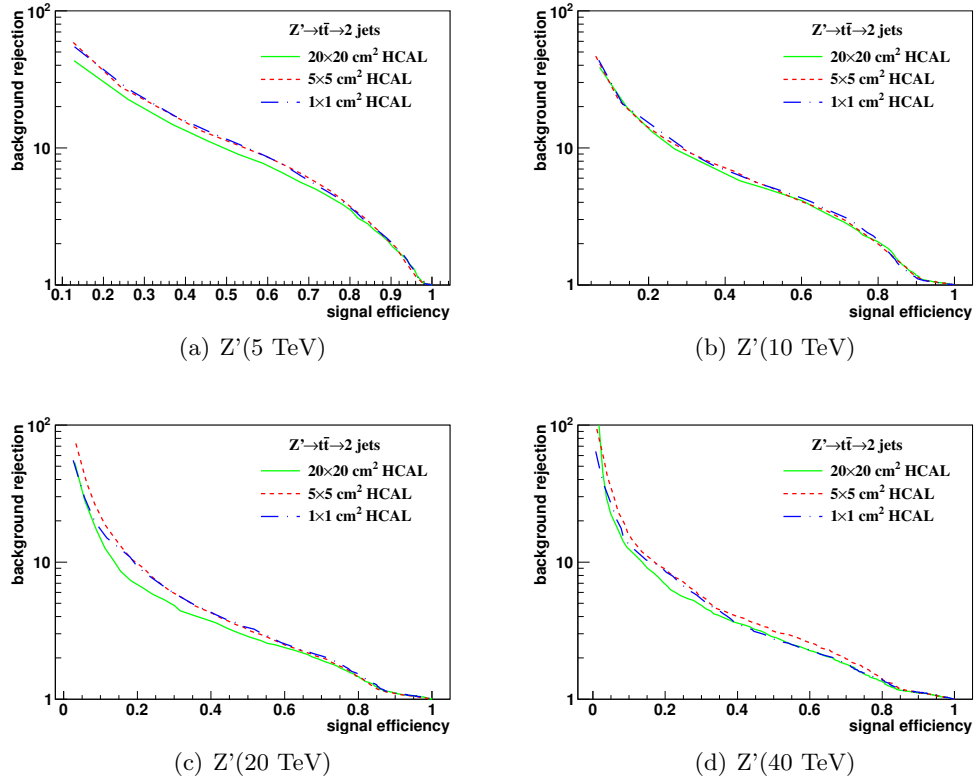


Figure 10: The ROC curves of soft drop mass selection for  $\beta = 2$  with resonance masses of 5, 10, 20 and 40 TeV. Three different detector cell sizes are compared:  $20 \times 20$ ,  $5 \times 5$  and  $1 \times 1 \text{ cm}^2$ . The signal (background) process is  $Z' \rightarrow t\bar{t}$  ( $Z' \rightarrow q\bar{q}$ ).

distance between the constituent  $k$  and the candidate subjet axis  $j$  in the  $y - \phi$  plane.  $R_0$  is the characteristic jet radius used in the anti- $k_t$  jet algorithm.

This analysis uses the jet reconstruction described in Sect. 2. The subjet axes are obtained by running the exclusive  $k_t$  algorithm [25] and reversing the last  $N$  clustering steps. Namely, when  $\tau_N$  is computed, the  $k_t$  algorithm is forced to return exactly  $N$  jets. If a large radius jet has  $N$  subjet(s), its  $\tau_N$  is smaller than  $\tau_{N-1}$ . Therefore, in our analysis, the ratios  $\tau_{21} \equiv \tau_2/\tau_1$  and  $\tau_{32} \equiv \tau_3/\tau_2$  are used to distinguish the one-prong background jets and the two-prong jets from  $W$  boson decays or the three-prong jets from top quark decays.

We use the ROC curves described in Sect. 4.2 to analyze the detector performance and determine the cell size that gives the best separation between signal and background processes. Following the suggestion of Ref. [26], the requirement on the soft drop mass with  $\beta = 0$  is applied before the study of  $N$ -subjettiness. For each detector configuration and resonance mass, the soft drop mass prerequisite window is determined as follows. The window is initialized by the median bin of the soft drop mass histogram from simulated signal events as described in Sect. 4.2. Comparing the adjacent bins, the bin with the larger number of events is included to extend the mass window iteratively. The procedure is repeated until the prerequisite mass window cut reaches a signal efficiency of 75%.

With this *a-priori* mass window pre-selection, the signal and background efficiencies of various  $\tau_{21}$  and  $\tau_{32}$  window cuts are scanned. Since some of the background distributions have long tails and leak into the signal-dominated region, we use the following method based on the Neyman-Pearson lemma to determine the  $\tau$  windows. First, we take the ratio of the signal to background  $\tau_{21}$  (or  $\tau_{32}$ ) histograms. The window is initialized by the bin with the maximum signal to background ratio (S/N). Comparing the adjacent bins, the bin with the larger S/N is included to extend the  $\tau_{21}$  (or  $\tau_{32}$ ) selection window. Every window has its corresponding  $\epsilon_{\text{sig}}$  and  $1/\epsilon_{\text{bkg}}$  and an ROC curve is mapped out.

In addition to the ROC curves, we use the so-called ‘‘Mann-Whitney’’ test [27] to quantify the detector performance. The value of the Mann-Whitney  $U$  variable is related to the area under the ROC curve; if the  $U$  value is bigger, it indicates the signal and background distributions have similar shapes and cannot be well-separated from each other. Vice versa, if the  $U$  value is smaller, we can achieve better signal and background separation.

Figures 11 and 13 show the distributions of  $\tau_{21}$  and  $\tau_{32}$  for  $M(Z') = 20$  TeV after applying the requirement on the soft drop mass. The signals considered are the  $Z' \rightarrow WW$  (for  $\tau_{21}$ ) and  $Z' \rightarrow t\bar{t}$  (for  $\tau_{32}$ ) processes. Figures 12 and 14 present the ROC curves from different detector cell sizes and resonance masses, respectively. The smallest detector cell size ( $1 \times 1 \text{ cm}^2$ ) does not have the best separation power. In fact, in some cases, the best separation power comes from a detector with bigger cell sizes ( $5 \times 5 \text{ cm}^2$  and  $20 \times 20 \text{ cm}^2$ ).

Figure 17 presents the summary plots of  $\tau_{21}$  and  $\tau_{32}$  with various detector cell sizes and resonance masses using the Mann-Whitney test. For  $\tau_{21}$  at smaller resonance masses, the detector performance improves when cell size is reduced. However, when the resonance mass increases, no improvement is observed using the smallest detector cell size ( $1 \times 1 \text{ cm}^2$ ). The case for  $\tau_{32}$  is similar to  $\tau_{21}$ . It is interesting to note that at

very large resonance masses, the large detector cell sizes ( $5 \times 5 \text{ cm}^2$  and  $20 \times 20 \text{ cm}^2$ ) have a better separation power than the smallest cell size considered in this analysis.

## 5.2. Energy correlation function

The energy correlation function (ECF) [28] is defined as follows:

$$ECF(N, \beta) = \sum_{i_1 < i_2 < \dots < i_N \in J} \left( \prod_{a=1}^N p_{Ti_a} \right) \left( \prod_{b=1}^{N-1} \prod_{c=b+1}^N R_{i_b i_c} \right)^\beta, \quad (3)$$

where the sum is over all constituents in jet  $J$ ,  $p_T$  is the transverse momentum of each constituent, and  $R_{mn}$  is the distance between two constituents  $m$  and  $n$  in the  $y$ - $\phi$  plane. In order to use a dimensionless variable, a parameter  $r_N$  is defined:

$$r_N^{(\beta)} \equiv \frac{ECF(N+1, \beta)}{ECF(N, \beta)}. \quad (4)$$

The idea of  $r_N$  comes from  $N$ -subjettiness  $\tau_N$ . Both  $r_N$  and  $\tau_N$  are linear in the energy of the soft radiation for a system of  $N$  partons accompanied by soft radiation. In general, if the system has  $N$  subjects,  $ECF(N+1, \beta)$  should be significantly smaller than  $ECF(N, \beta)$ . Therefore, we can use this feature to distinguish jets with different numbers of subjects. As in Sect. 5.1, the ratio  $r_N/r_{N-1}$ , denoted by  $C_N$ , (double-ratios of ECFs) is used to study the detector performance:

$$C_N^{(\beta)} \equiv \frac{r_N^{(\beta)}}{r_{N-1}^{(\beta)}} = \frac{ECF(N-1, \beta) ECF(N+1, \beta)}{ECF(N, \beta)^2}. \quad (5)$$

In our analysis, we set  $N = 2$  and  $\beta = 1$  ( $C_2^1$ ).

Figure 15 presents the histograms of  $C_2^1$  with  $M(Z') = 20 \text{ TeV}$  after making the requirement on the soft drop mass. The signal considered is the  $Z' \rightarrow WW$  process. Figure 16 shows the ROC curves from different detector cell sizes for each resonance mass. One can see that the smallest detector cell size ( $1 \times 1 \text{ cm}^2$ ) does not have the best signal-to-background separation power. Figure 17 summarizes the result of the Mann-Whitney test for  $C_2^1$ . When the resonance mass increases, no improvement is observed with the smallest cell size.

## 6. Conclusions

The studies presented in this paper show that the reconstruction of jet substructure variables for future particle colliders will benefit from small cell sizes of the hadronic calorimeters. This conclusion was obtained using the realistic GEANT4 simulation of calorimeter response combined with reconstruction of calorimeter clusters used as inputs for jet reconstruction. Hadronic calorimeters that use the cell sizes of  $20 \times 20 \text{ cm}^2$  ( $\Delta\eta \times \Delta\phi = 0.087 \times 0.087$ ) are least performant for almost every substructure variable considered in this analysis, for jet transverse momenta between 2.5 and 10 TeV. Such cell sizes are similar to those used for the ATLAS and CMS detectors at the LHC. In terms of reconstruction of physics-motivated quantities used for jet substructure studies, the performance of a hadronic calorimeter with  $\Delta\eta \times \Delta\phi = 0.022 \times 0.022$  is, in

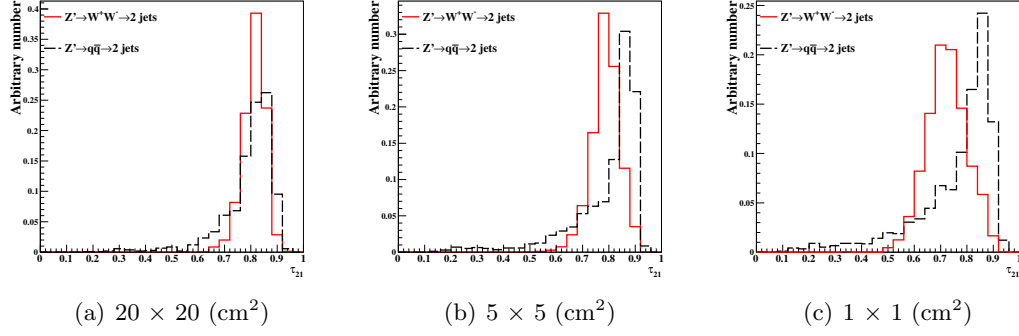


Figure 11: Distributions of  $\tau_{21}$  for  $M(Z') = 20 \text{ TeV}$  for different detector granularities. Cell sizes of  $20 \times 20$ ,  $5 \times 5$ , and  $1 \times 1 \text{ cm}^2$  are shown here.

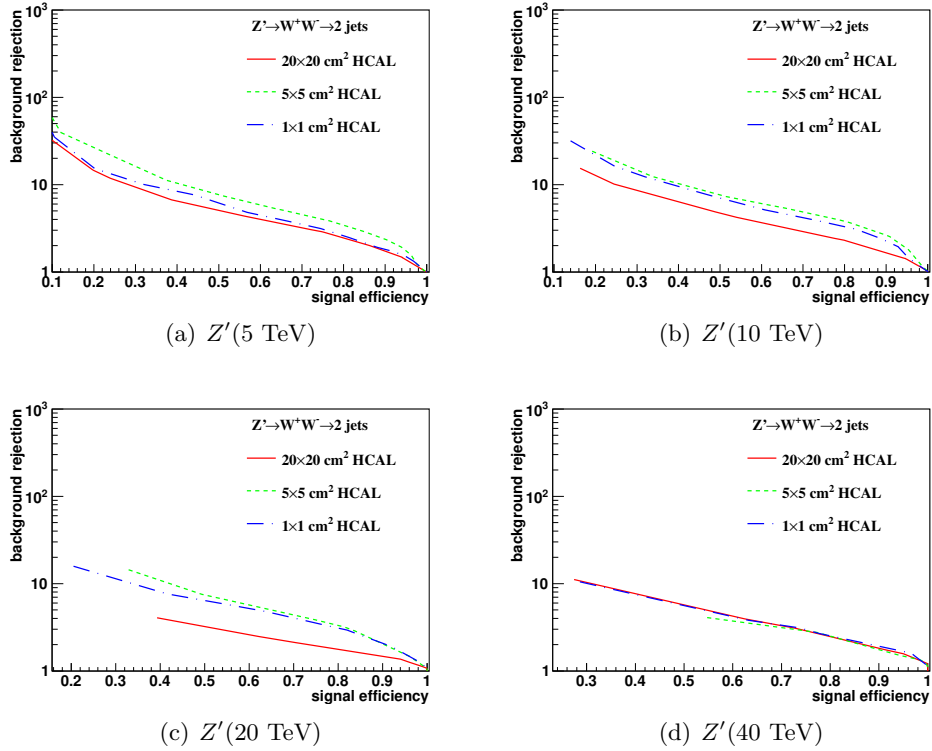


Figure 12: Signal efficiency versus background rejection rate using  $\tau_{21}$ . Resonance masses of (a) 5 TeV, (b) 10 TeV, (c) 20 TeV and (d) 40 TeV are shown here. In each figure, the three ROC curves correspond to different cell sizes.

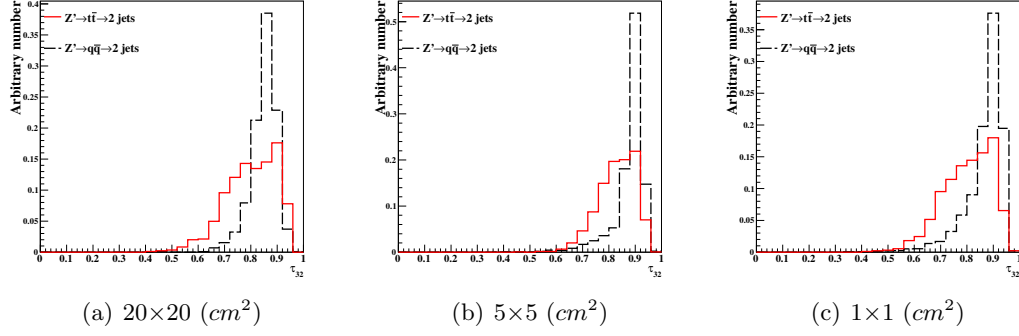


Figure 13: Distributions of  $\tau_{32}$  for  $M(Z') = 20$  TeV for different detector granularities. Cell sizes of  $20 \times 20$ ,  $5 \times 5$ , and  $1 \times 1$   $\text{cm}^2$  are shown here.

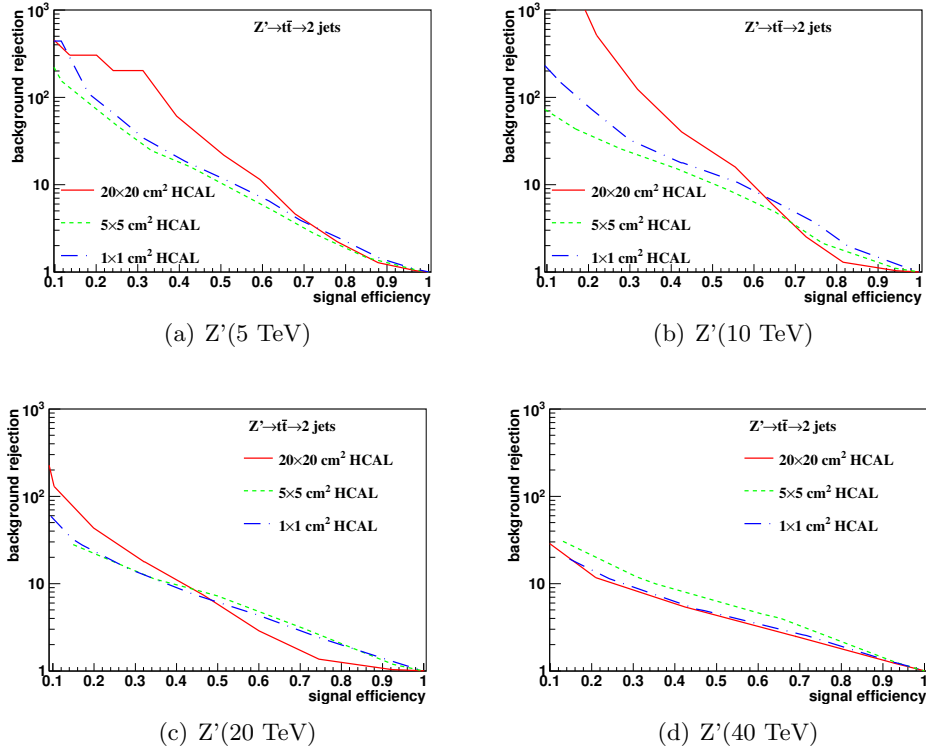


Figure 14: Signal efficiency versus background rejection rate using  $\tau_{32}$ . Resonance masses of (a) 5 TeV, (b) 10 TeV, (c) 20 TeV and (d) 40 TeV are shown here. In each figure, the three ROC curves correspond to different HCAL cell sizes.

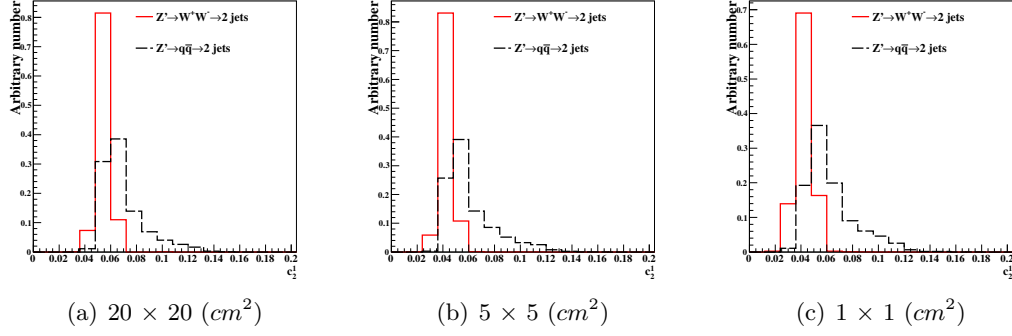


Figure 15: Distributions of  $C_2^1$  with  $M(Z') = 20 \text{ TeV}$  for different detector granularities. Cell sizes of  $20 \times 20$ ,  $5 \times 5$ , and  $1 \times 1 \text{ cm}^2$  are shown here.

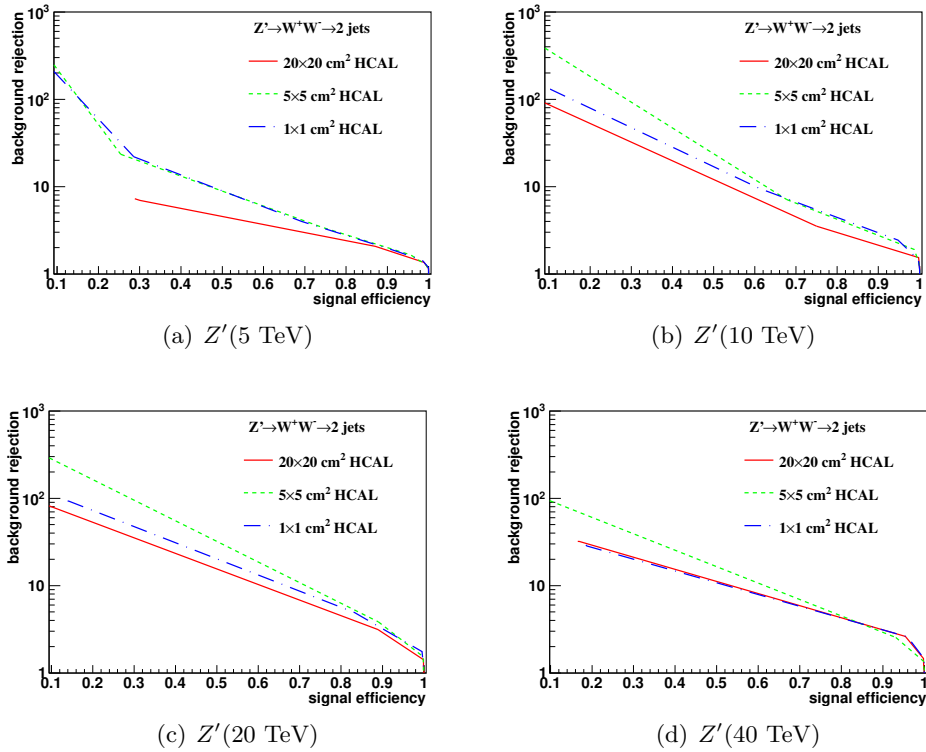


Figure 16: Signal efficiency versus background rejection rate using  $C_2^1$ . The resonance masses of (a) 5 TeV, (b) 10 TeV, (c) 20 TeV, and (d) 40 TeV are shown here. In each figure, the three ROC curves correspond to different detector sizes.



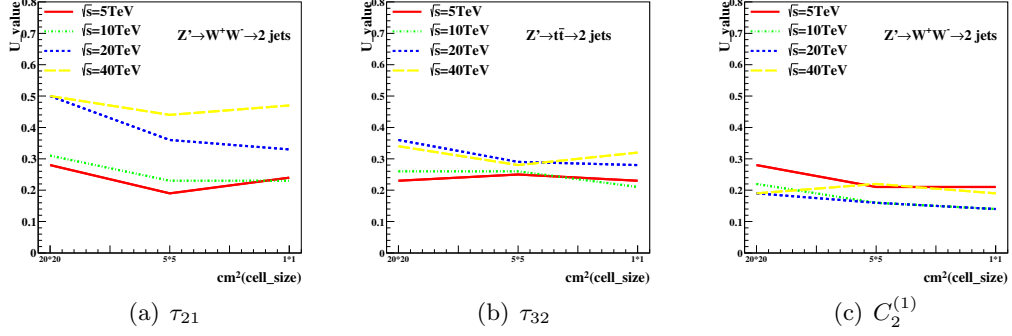


Figure 17: The Mann-Whitney  $U$  values for  $\tau_{21}$ ,  $\tau_{32}$ , and  $C_2^{(1)}$  reconstructed for different resonance masses and detector cell sizes.

most cases, better than for a detector with  $0.087 \times 0.087$  cells. The performance of the HCAL with cells  $\Delta\eta \times \Delta\phi = 0.0087 \times 0.0087$  and  $\Delta\eta \times \Delta\phi = 0.0043 \times 0.0043$  was found to be similar.

Thus this study confirms the HCAL geometry of the SiFCC detector [7], with the  $\Delta\eta \times \Delta\phi = 0.022 \times 0.022$  HCAL cells. It also confirms the HCAL design of the baseline FCC-hh [19, 20] detector with  $\Delta\eta \times \Delta\phi = 0.025 \times 0.025$  HCAL cells.

It interesting to note that, for very boosted jets with transverse momenta close to 20 TeV, no significant improvement with the decrease of cell sizes was observed. This result needs to be understood in terms of various types of simulations and different options for reconstruction of the calorimeter clusters.

## Acknowledgements

This research was performed using resources provided by the Open Science Grid, which is supported by the National Science Foundation and the U.S. Department of Energy Office of Science. We gratefully acknowledge the computing resources provided on Blues, a high-performance computing cluster operated by the Laboratory Computing Resource Center at Argonne National Laboratory. Argonne National Laboratory is supported by the U.S. Department of Energy, Office of Science, Office of High Energy Physics under contract DE-AC02-06CH11357. The Fermi National Accelerator Laboratory (Fermilab) is operated by Fermi Research Alliance, LLC under Contract No. DE-AC02-07CH11359 with the United States Department of Energy.

## 258 References

- 259 [1] M. Benedikt, [The Global Future Circular Colliders Effort](#) CERN-ACC-SLIDES-2016-0016. Pre-  
260 sented at P5 Workshop on the Future of High Energy Physics, BNL, USA, Dec. 15-18, 2013.  
261 URL <http://cds.cern.ch/record/2206376>
- 262 [2] J. Tang, et al., Concept for a Future Super Proton-Proton Collider (2015). [arXiv:1507.03224](#).
- 263 [3] R. Calkins, et al., [Reconstructing top quarks at the upgraded LHC and at future accelerators](#),  
264 in: Proceedings, Community Summer Study 2013: Snowmass on the Mississippi (CSS2013): Min-  
265 neapolis, MN, USA, July 29-August 6, 2013. [arXiv:1307.6908](#).  
266 URL <https://inspirehep.net/record/1244676/files/arXiv:1307.6908.pdf>
- 267 [4] S. V. Chekanov, J. Dull, Energy range of hadronic calorimeter towers and cells for high-pT jets  
268 at a 100 TeV collider. [arXiv:1511.01468](#).
- 269 [5] E. Coleman, M. Freytsis, A. Hinzmann, M. Narain, J. Thaler, N. Tran, C. Vernieri, The importance  
270 of calorimetry for highly-boosted jet substructure [arXiv:1709.08705](#).
- 271 [6] DELPHES 3 Collaboration, J. de Favereau, C. Delaere, P. Demin, A. Giammanco, V. Lematre,  
272 A. Mertens, M. Selvaggi, DELPHES 3, A modular framework for fast simulation of a generic  
273 collider experiment, JHEP 02 (2014) 057. [arXiv:1307.6346](#), [doi:10.1007/JHEP02\(2014\)057](#).
- 274 [7] S. V. Chekanov, M. Beydler, A. V. Kotwal, L. Gray, S. Sen, N. V. Tran, S. S. Yu, J. Zuzelski, Initial  
275 performance studies of a general-purpose detector for multi-TeV physics at a 100 TeV pp collider,  
276 JINST 12 (06) (2017) P06009. [arXiv:1612.07291](#), [doi:10.1088/1748-0221/12/06/P06009](#).
- 277 [8] J. Allison, et al., Recent developments in Geant4, Nuclear Instruments and Methods in Physics  
278 Research A 835 (2016) 186.
- 279 [9] M. J. Charles, PFA Performance for SiD, in: Linear colliders. Proceedings, International Linear  
280 Collider Workshop, LCWS08, and International Linear Collider Meeting, ILC08, Chicago, USA,  
281 November 16-20, 2008 , 2009. [arXiv:0901.4670](#).
- 282 [10] J. S. Marshall, M. A. Thomson, Pandora Particle Flow Algorithm, in: Proceedings, International  
283 Conference on Calorimetry for the High Energy Frontier (CHEF 2013), 2013, pp. 305–315. [arXiv:](#)  
284 [1308.4537](#).
- 285 [11] G. P. S. M. Cacciari, G. Soyez, FastJet user manual CERN-PH-TH/2011-297. [arXiv:1111.6097](#).
- 286 [12] M. Cacciari, G. P. Salam, G. Soyez, The anti-kt jet clustering algorithm, JHEP 0804 (2008) 063.  
287 [arXiv:0802.1189](#).
- 288 [13] S. Chekanov, HepSim: a repository with predictions for high-energy physics experiments, Advances  
289 in High Energy Physics 2015 (2015) 136093, available as <http://atlaswww.hep.anl.gov/hepsim/>.
- 290 [14] B. Auerbach, S. Chekanov, J. Love, J. Proudfoot, A. Kotwal, Sensitivity to new high-mass states  
291 decaying to  $t\bar{t}b\bar{a}$  at a 100 TeV collider [arXiv:1412.5951](#).
- 292 [15] J. Butterworth, B. Cox, J. R. Forshaw,  $WW$  scattering at the CERN LHC, Phys.Rev. D65 (2002)  
293 096014. [arXiv:hep-ph/0201098](#), [doi:10.1103/PhysRevD.65.096014](#).
- 294 [16] S. Catani, Y. L. Dokshitzer, M. H. Seymour, B. R. Webber, [Longitudinally-invariant k-clustering](#)  
295 [algorithms for hadron-hadron collisions](#), Nuclear Physics B 406 (12) (1993) 187 – 224.  
296 URL <http://www.sciencedirect.com/science/article/pii/055032139390166M>
- 297 [17] S. D. Ellis, D. E. Soper, Successive combination jet algorithm for hadron collisions, Phys. Rev.  
298 D48 (1993) 3160–3166. [arXiv:hep-ph/9305266](#), [doi:10.1103/PhysRevD.48.3160](#).
- 299 [18] ATLAS Collaboration Collaboration, G. Aad, et al., Jet mass and substructure of inclusive jets in  
300  $\sqrt{s} = 7$  TeV  $pp$  collisions with the ATLAS experiment, JHEP 1205 (2012) 128. [arXiv:1203.4606](#),  
301 [doi:10.1007/JHEP05\(2012\)128](#).
- 302 [19] C. Neubüser, Performance studies and requirements on the calorimeters for a fcc-hh experiment,  
303 in: Z.-A. Liu (Ed.), Proceedings of International Conference on Technology and Instrumentation  
304 in Particle Physics 2017, Springer Singapore, Singapore, 2018, pp. 37–43.
- 305 [20] J. Faltova, [Design and performance studies of a hadronic calorimeter for a fcc-hh experiment](#),  
306 Journal of Instrumentation 13 (03) (2018) C03016.  
307 URL <http://stacks.iop.org/1748-0221/13/i=03/a=C03016>
- 308 [21] A. J. Larkoski, S. Marzani, G. Soyez, J. Thaler, Soft Drop, JHEP 05 (2014) 146. [arXiv:1402.2657](#),  
309 [doi:10.1007/JHEP05\(2014\)146](#).
- 310 [22] Y. L. Dokshitzer, G. D. Leder, S. Moretti, B. R. Webber, Better jet clustering algorithms, JHEP  
311 08 (1997) 001. [arXiv:hep-ph/9707323](#), [doi:10.1088/1126-6708/1997/08/001](#).
- 312 [23] M. Wobisch, T. Wengler, Hadronization corrections to jet cross-sections in deep inelastic scattering,

- in: Monte Carlo generators for HERA physics. Proceedings, Workshop, Hamburg, Germany, 1998-1999, 1998, pp. 270–279. [arXiv:hep-ph/9907280](#).
- [24] J. Thaler, K. Van Tilburg, Identifying Boosted Objects with N-subjettiness, JHEP 03 (2011) 015. [arXiv:1011.2268](#), [doi:10.1007/JHEP03\(2011\)015](#).
- [25] S. Catani, Y. L. Dokshitzer, M. H. Seymour, B. R. Webber, Longitudinally-invariant  $k_{\perp}$ -clustering algorithms for hadron-hadron collisions, Nucl. Phys. B 406 (CERN-TH-6775-93. LU-TP-93-2) (1993) 187–224.
- [26] F. A. Dreyer, L. Necib, G. Soyez, J. Thaler, Recursive Soft Drop, JHEP 06 (2018) 093. [arXiv:1804.03657](#), [doi:10.1007/JHEP06\(2018\)093](#).
- [27] H. B. Mann, D. R. Whitney, [On a test of whether one of two random variables is stochastically larger than the other](#), Ann. Math. Statist. 18 (1) (1947) 50–60. [doi:10.1214/aoms/1177730491](#). URL <https://doi.org/10.1214/aoms/1177730491>
- [28] A. J. Larkoski, G. P. Salam, J. Thaler, Energy Correlation Functions for Jet Substructure, JHEP 06 (2013) 108. [arXiv:1305.0007](#), [doi:10.1007/JHEP06\(2013\)108](#).